Electronic Supplementary Material (ESI) for Lab on a Chip.

Supplementary information

Deformation of leukaemia cell lines in hyperbolic microchannels: investigating the role of shear and extensional components

Monica Piergiovanni, Valeria Galli, Gregor Holzner, Stavros Stavrakis, Andrew deMello, Gabriele Dubini

SUPPLEMENTARY NOTES

Supplementary Note 1.
Image processing method

All images were processed by means of a Python code that operated according to the following steps (Supplementary Figure S2):

- Background calculation and subtraction: background was calculated as the arithmetic average of each pixel in a desired number of images from each folder (the higher this number, the more accurate the background image, but the slower the processing);
- Bandpass filtering of the pixel intensity distribution: upper and lower thresholds were chosen depending on the image brightness - this band should be moved towards lower values for very dark image and vice versa;
- Image smoothing: an image blurring algorithm (cv2.medianBlur) was used to remove high frequency components such as edges and noise;
- Filtering: a combination of two algorithms (open CV binary and Otsu thresholding) was performed. The Otsu method is particularly useful in the case of bimodal images, (two main colours are present) where the pixel intensity histogram presents two separate peaks. The Otsu method automatically detects the separation of the two parts of the histogram so that the binary thresholding works efficiently on both.
- Erosion and dilation: these are standard morphological transformation applied to get smoother boundaries;
- Contour tracking: an openCV algorithm for contour finding was applied (cv2.findContours);
- Parameters calculations and saving: with regards to the detected contours, area, perimeter, width, height and x,y coordinates of the centroid were computed and saved in a Comma Separated Value (.csv) file

Supplementary Note 2.
CFD simulations

A number of fluid dynamic simulations were performed to support the experimental campaign, to assess the variation of the main parameters of interest (velocity, shear stress, extensional rate and pressure) in different geometrical and rheological scenarios. The fluid dynamic forces acting on this scenario are of two main natures: a shear component prominent close to the channel walls and an extensional component dominating the behaviour along the channel centreline. Shear induces both rotation and deformation, whereas extension implies a (uniaxial) stretching along the direction of the flow. Since the final devices with the sheath system were almost 3 cm long, it was convenient to study the upstream sheath system and the channel part separately: a sufficiently fine mesh (with elements down to 2 μm in size) with the whole geometry would have had millions of elements with severe impact on calculation time. Therefore, four geometries were meshed and used in simulations:

- upstream part (sheath flow system), to calculate the correct inlet boundary conditions of the sheath and main flows to be used in the channel parts;
- straight channel, Lc = 300 μm;
- short hyperbolic channel, Lc = 500 μm;
- long hyperbolic channel, Lc = 1000 μm.

ANSYS Mesher was used to build a structured Cartesian mesh (*i.e.,* a mesh composed by hexahedral elements only), which is often deemed the optimal solution for simple geometries, providing maximum orthogonality, minimum skewness and high element quality. In the initial region of the hyperbola this was hardly feasible due to the curved conformation, thus an unstructured mesh with minimum skewness and aspect ratio was chosen. The key regions where a fine and high quality mesh is needed are the junction for the upstream sheath flow module, the whole channel for the straight geometry and the contraction (point of minimum width, y = $w_c/2$) for the hyperbolic channels.
After a sensitivity analysis, the mesh size was determined to be of 2 μm for the hyperbolic channels and of 4 μm for the straight channel (Supplementary Figure S3).
For each channel, the inlet velocity profile corresponded to the outlet velocity profile of the upstream sheath flow system at every tested flow rates, accordingly with the experimental data. Steady-state simulations with pressure based solver and laminar flow regime were set.
The fluids rheological properties were defined to match with the Buffer 0.25 and Buffer 0.50 used in the experimental campaign. Both have a shear thinning behaviour, which could be modelled by fitting the power law model with appropriate indices

$$\tau = K \cdot \dot{\gamma}^{n-1}$$

where τ is the shear stress, $\dot{\gamma}$ is the the shear rate, *K* is the consistency index and *n* is the power index. The software also requires upper and lower bounds of the viscosity values: for Buffer 0.50 these were found in the literature, whereas for Buffer 0.25 they were taken from the rheological characterization with the Couette rheometer (data not shown).

Supplementary note 3.
Literature data on droplet deformation.
Previous studies have focused either on micron-sized droplet deformability [12] or comparisons between droplets, air bubbles and red blood cells [9]. Since red blood cells lack the nucleus, the deformation behaviour for these cells and liquid droplets can be assumed to be similar.
For nucleated cells, on the contrary, computational models have been used to assess the issue of different viscosities of the nucleus and cytoplasm. Kaoui and co-workers studied the 2D dynamics of a bilamellar vesicle under shear flow and investigated how the dynamic and rheological properties of a leukocyte are affected by the size and deformability of the nucleus as well as the amount of fluid enclosed between the nucleus and the cell. Importantly, this model failed to describe cell behaviour as a bilamellar vesicle, which inherently does not contain an internal structure. This is because leukocytes adapt their mechanical properties and act as a solid or as a liquid depending on how they are deformed by the imposed fluid. [11]. Another study demonstrated dynamic nuclear deformation as cells migrate through confined spaces, revealing distinct phases of nuclear translocation through constriction [10]. However, since this study addresses dynamic changes that occur during cell migration, it cannot be directly compared with experiments on cell deformation in flow.

SUPPLEMENTARY FIGURES

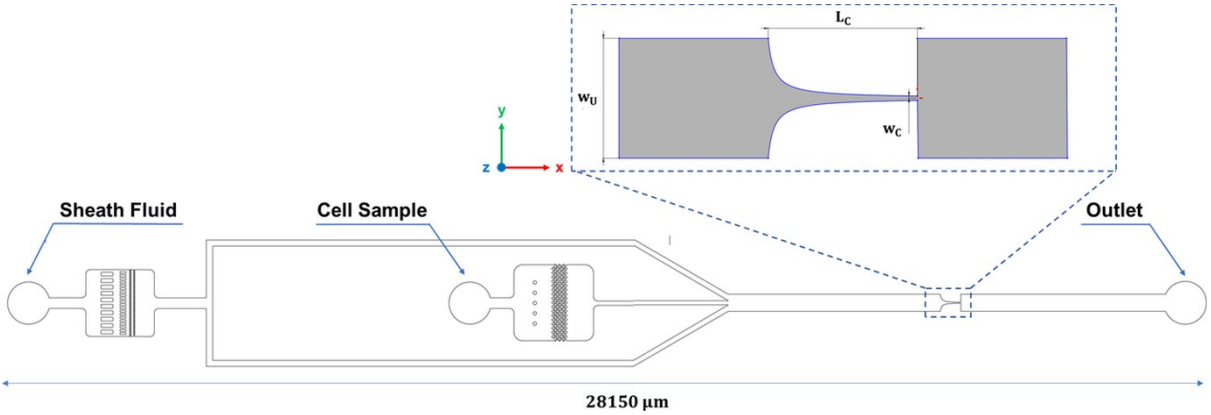

Supplementary Figure S1: *Geometry of the hyperbolic channels: configuration with sheath flow and filters. Hyperbolic channel with dimensions (inset).*

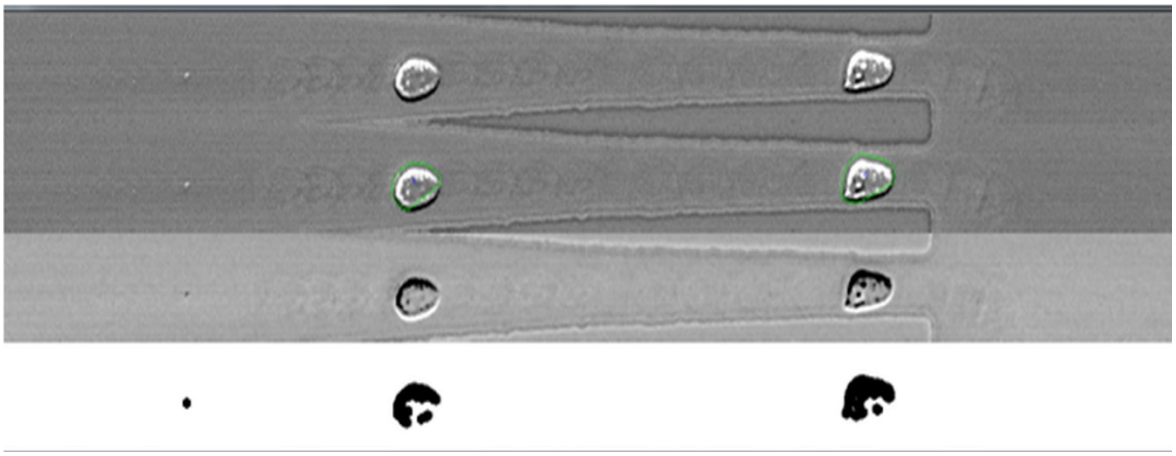

Supplementary Figure S2: *Representation of the image processing steps. The image shows the output of the image processing code (top to bottom): raw image, contours calculation, image downstream all the morphological operations and binary image.*

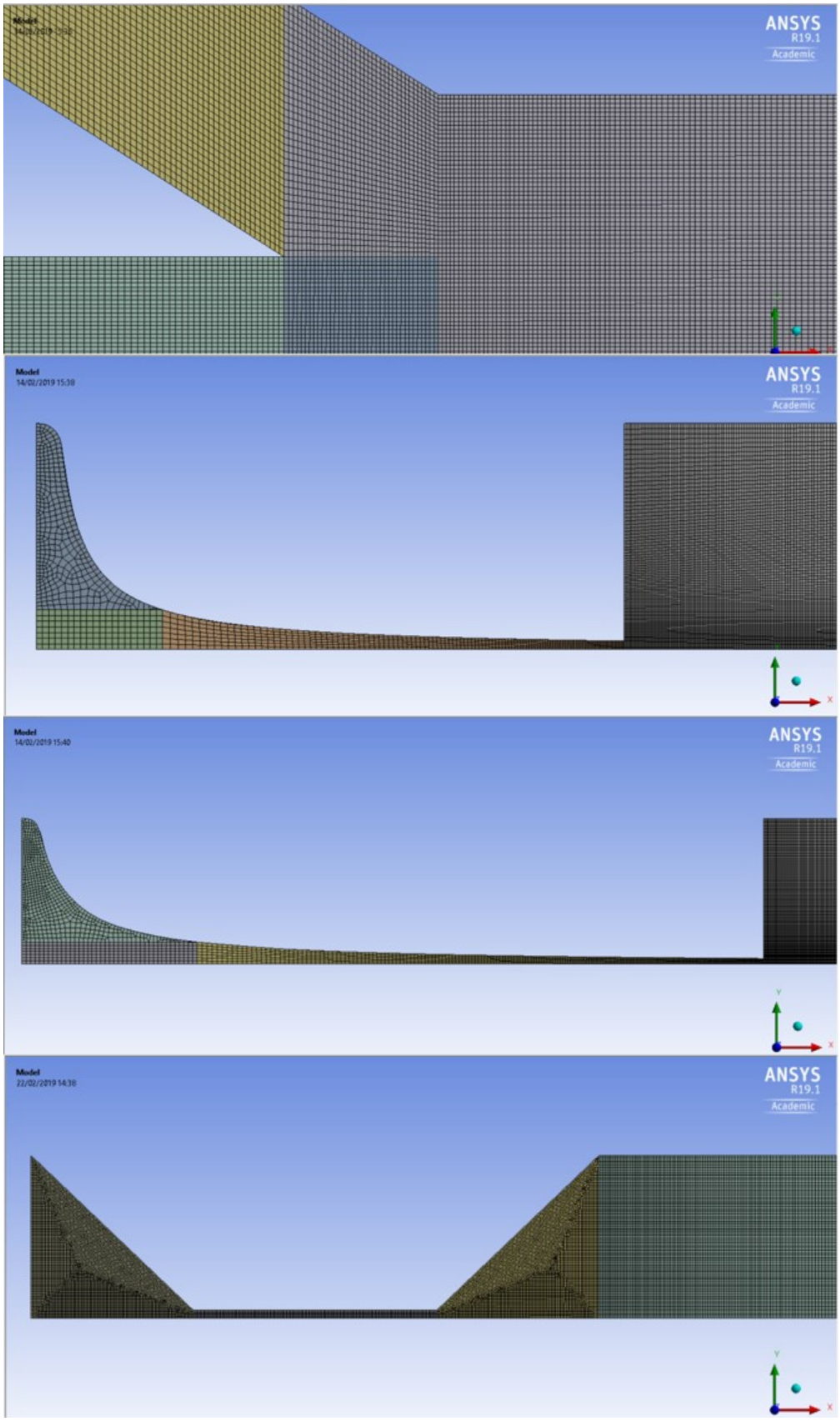

Supplementary Figure S3: *Overview of the four meshes (from top to bottom): upstream (detail at junction), hyperbolic with Lc = 500 µm, hyperbolic with Lc =1000 µm, straight channel.*

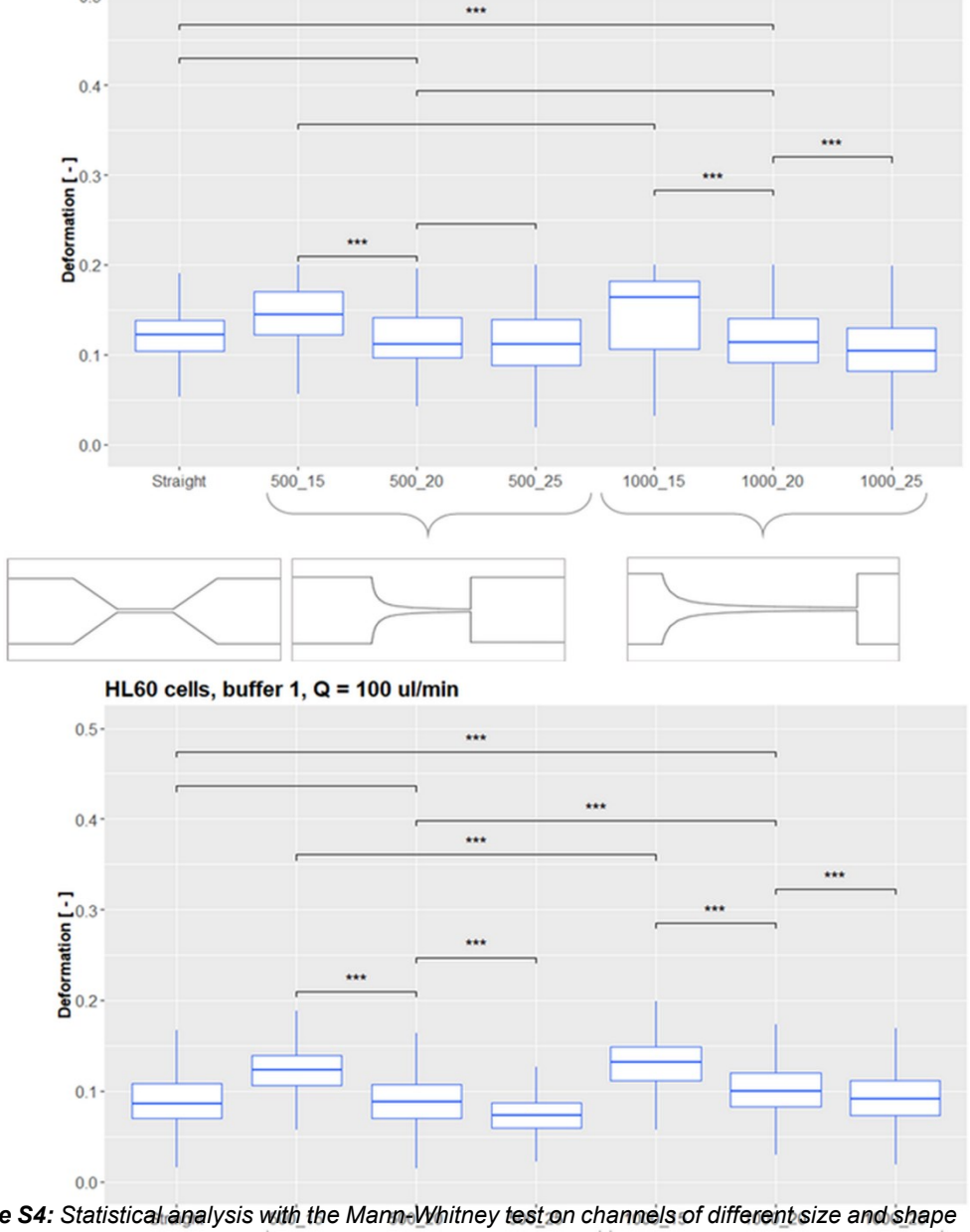

Supplementary Figure S4: *Statistical analysis with the Mann-Whitney test on channels of different size and shape for HL60 (top) and Jurkat (bottom) with the less viscous buffer at the maximum flow rate. (*** : p < 0,001, no stars: not significant).*

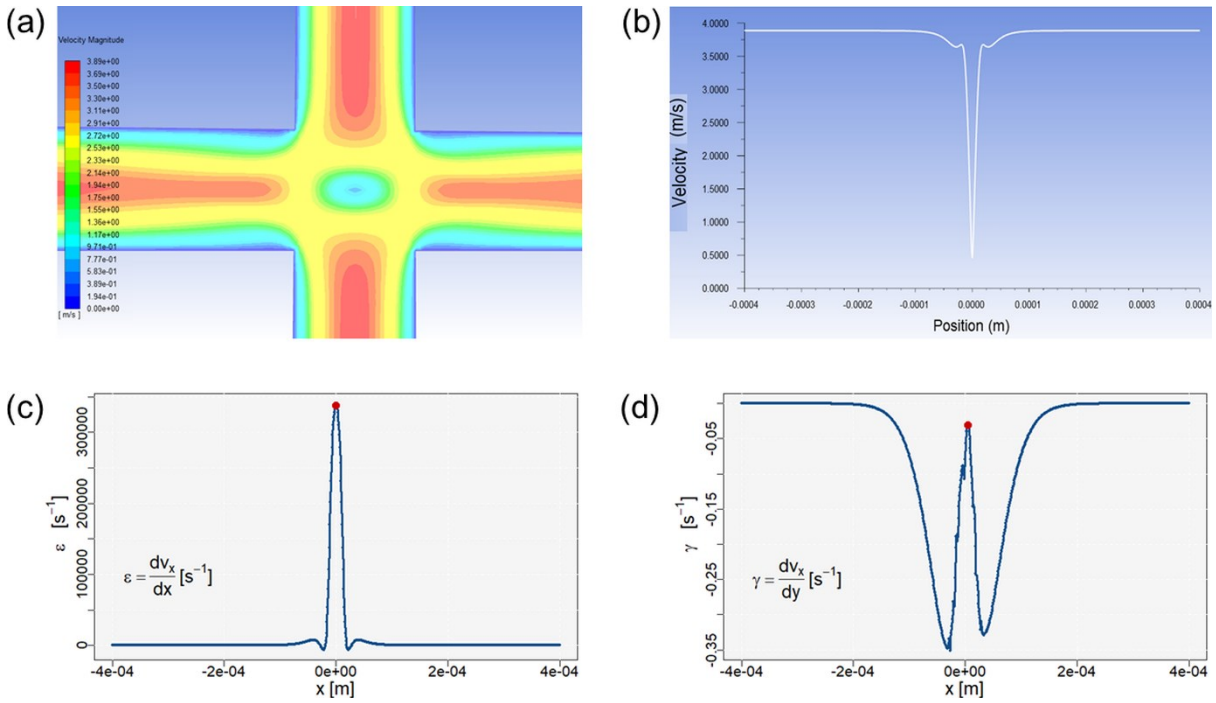

***Supplementary Figure S5**: Fluid dynamic parameters in the cross shaped device and respective profiles along the centrelines (right panel): velocity (a), extensional rate (b) and shear rate (c). Data reported refer to 90 µl/min.*

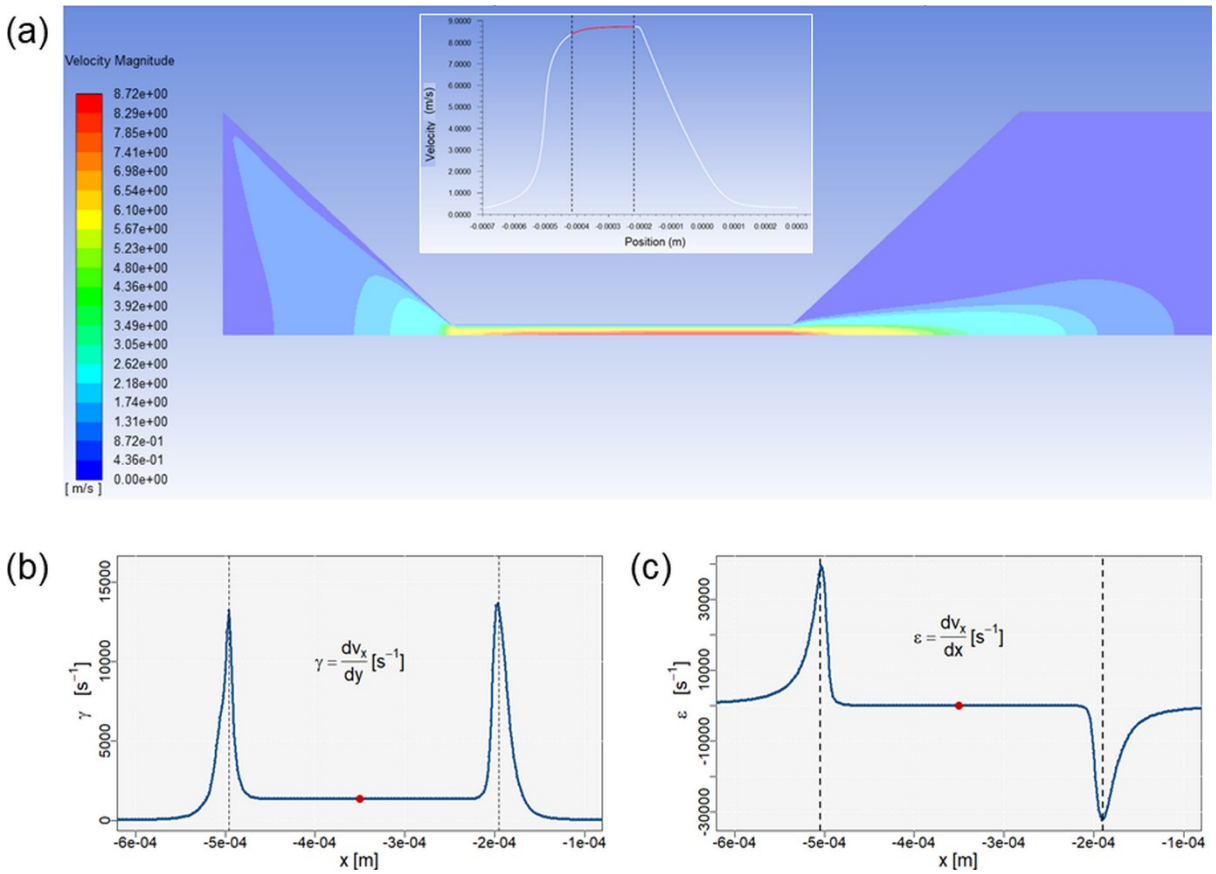

***Supplementary Figure S6**: Fluid dynamic parameters in the straight channel: velocity contours and profile along the centreline in the inset (a), extensional rate (b) and shear rate (c) along the centreline with red dots showing representative values taken for each case. Data reported refer to 100 µl/min.*

SUPPLEMENTARY TABLES

***Supplementary Table S1**: Dimensions of the all the channels.*

	$L_C\,[\mu m]$	$w_u\,[\mu m]$	$w_C\,[\mu m]$	$h\,[\mu m]$
Short hyperbolic	500	400	15	20
	500	400	20	20
	500	400	25	20
Long hyperbolic	1000	400	15	20
	1000	400	20	20
	1000	400	25	20
Straight	300	400	20	20
Cross	-	20	20	20

***Supplementary Table S2**: Literature values of Jurkat and HL60 mechanical properties. S and G1 refer to the cell cycle phase*

	Parameter	**Mean**	**SD**	**Method**	**Ref**
Jurkat cells	$\mu\,[Pa \cdot s]$	4.1	2.7	Micropipette	[1]
	$\mu\,[Pa \cdot s]$	3.5	2	Micropipette	[2]
	$E\,[Pa]$	20	-	AFM	[3]
	$E\,[Pa]$	48	35	AFM	[4]
	$E\,[Pa]$	510	60	AFM	[5]
HL60 cells	$\mu\,[Pa \cdot s]$	333.5	26	Optical Stretcher	[6]
	$\mu\,[Pa \cdot s]$	276	14	Micropipette	[7]
	$\mu\,[Pa \cdot s]$	197	25	Micropipette	[7]
	$E\,[Pa]$	855	670	AFM	[4]
		Min	**Max**		
	$E\,[Pa]$	280	2100	Micropipette	[8]
White Blood Cells					
Neutrophils	$\mu\,[Pa \cdot s]$	212.5	43.3	Optical Stretcher	[6]
Macrophages	$\mu\,[Pa \cdot s]$	174	10.2	Optical Stretcher	[6]
Monocytes	$\mu\,[Pa \cdot s]$	142.1	44.7	Optical Stretcher	[6]
Neutrophils	$E\,[Pa]$	156	87	AFM	[4]
Lymphocytes	$E\,[Pa]$	1240	90	AFM	[5]

BIBLIOGRAPHY (for Supplementary Information)

1. Chen, K. *et al.* Influence of expressed TRAIL on biophysical properties of the human leukemic cell line Jurkat. *Cell Res.* **14**, 161–168 (2004).
2. Tozeren, A. *et al.* Micromanipulation of adhesion of a Jurkat cell to a planar bilayer membrane containing lymphocyte function-associated antigen 3 molecules. *J. Cell Biol.* **116**, 997–1006 (1992).
3. Schmitz, J., Benoit, M. & Gottschalk, K. E. The viscoelasticity of membrane tethers and its importance for cell adhesion. *Biophys. J.* **95**, 1448–1459 (2008).
4. Rosenbluth, M. J., Lam, W. A. & Fletcher, D. A. Force microscopy of nonadherent cells: a comparison of leukemia cell deformability. *Biophys. J.* **90**, 2994–3003 (2006).
5. Cai, X. *et al.* Connection between biomechanics and cytoskeleton structure of lymphocyte and Jurkat cells: An AFM study. *Micron* **41**, 257–262 (2010).
6. Ekpenyong, A. E. *et al.* Viscoelastic Properties of Differentiating Blood Cells Are Fate- and Function-Dependent. *PLoS One* **7**, (2012).
7. Tsai, M. A., Waugh, R. E. & Keng, P. C. Cell cycle-dependence of HL-60 cell deformability. *Biophys. J.* **70**, 2023–2029 (1996).
8. Hallows, K. R. & Frank, R. S. Changes in mechanical properties with DMSO-induced differentiation of HL-60 cells. *Biorheology* **29**, 295–309 (1992).
9. David Bento, Raquel O. Rodrigues, Vera Faustino, Diana Pinho, Carla S. Fernandes, Ana I. Pereira, Valdemar Garcia, João M. Miranda and Rui Lima “Deformation of Red Blood Cells, Air Bubbles, and Droplets in Microfluidic Devices: Flow Visualizations and Measurements” Micromachines 2018, 9, 151
10. Patricia M. Davidson, Josiah Sliz, Philipp Isermann, Celine Denais and Jan Lammerding, “Design of a microfluidic device to quantify dynamic intra-nuclear deformation during cell migration through confining environments”, Integr Biol (Camb). 2015 Dec;7(12):1534-4
11. Badr Kaoui, Timm Krüger and Jens Harting, “Complex Dynamics of a Bilamellar Vesicle as a Simple Model for Leukocytes”, Soft Matter, 2013,9, 8057-8061
12. Camilo Ulloa, Alberto Ahumada and Marıa Luisa Cordero, “The effect of confinement on the deformation of microfluidic drops”, Phys Rev E Stat Nonlin Soft Matter Phys. 2014 Mar; 89(3):033004